Quantifying 3D Crack Propagation in Nodular Graphite Cast Iron Using Advanced Digital Volume Correlation and X-ray Computed Tomography

Haizhou Liu, François Hild

Quantifying 3D Crack Propagation in Nodular Graphite Cast Iron Using Advanced Digital Volume Correlation and X-ray Computed Tomography

Haizhou Liu,[1] François Hild[1*]

[1]*Université Paris-Saclay, CentraleSupélec, ENS Paris-Saclay, CNRS*

LMPS – Laboratoire de Mécanique Paris-Saclay

Gif-sur-Yvette, France

*Corresponding author**:** François Hild, E-mail: Francois.HILD@ens-paris-saclay.fr

Highlights

- Advanced DVC to quantify 3D crack shape and its propagation
- Deformation analysis reveals crack tearing, plastic zones, and strain concentrations
- CODs display crack opening variations and the entire cracking process
- SIF estimation shows dominance of mode I stress

Graphical abstract

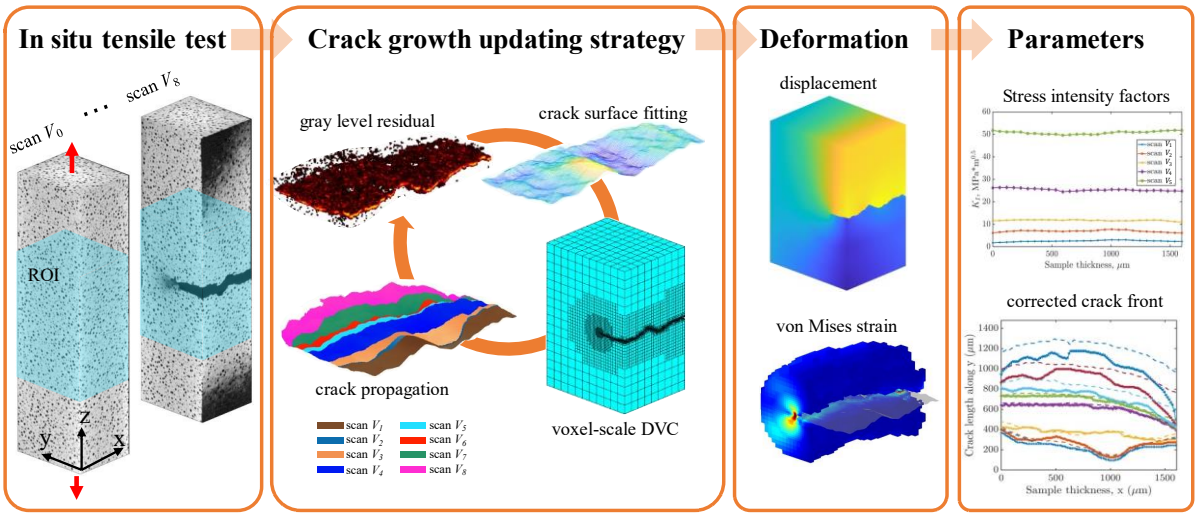

Abstract

Advanced digital volume correlation (DVC) combined with X-ray computed tomography (XCT) was utilized to investigate the 3D crack propagation in nodular graphite cast iron under tensile loading. The objective of this work was to quantify crack growth at the voxel-scale and

extract fracture mechanics parameters such as the 3D crack front, crack opening displacements (CODs), and stress intensity factors (SIFs). By employing a crack growth updating strategy and an adaptive multiscale mesh, the 3D crack shape and propagation were accurately captured throughout the entire process. Von Mises strain and COD fields were characterized to provide insights into plastic zones and variations in crack opening behavior. Estimation of SIFs revealed a mode I dominant regime and limited influence from modes II and III. This study provides comprehensive insights into crack propagation and crack opening behavior, providing valuable information to fracture mechanics.

Keywords: digital volume correlation, 3D crack propagation, 3D crack shape, stress intensity factor, nodular graphite cast iron

1. Introduction

Nodular graphite cast iron, also known as ductile iron, has been widely recognized and utilized across various industries, including automotive, wind power, and heavy machinery, due to its unique combination of strength, ductility, and fatigue resistance [1]. In these applications, the components made of such material are often subjected to cyclic loading, leading to the initiation and propagation of fatigue cracks, which seriously affect the in-service life. The growth of fatigue cracks in materials is often evaluated using the well-known Paris' law [2], which establishes a relationship between the stress intensity factor range and the crack growth rate. As a consequence, it is crucial to monitor fatigue crack propagation and measure stress intensity factors (SIFs) for calibrating predictive models.

In the case of two-dimensional (2D) images, digital image correlation (DIC) has gained popularity in experimental and fracture mechanics applications. DIC enables for full-field measurements near crack tips, allowing for the estimation of fracture mechanics parameters such as crack opening displacement (COD) [3], energy release rate [4], and stress intensity factors (SIFs) [5, 6]. However, when dealing with three-dimensional (3D) crack propagation in thick samples [7], relying solely on 2D measurements of CODs and SIFs fails to provide a comprehensive understanding of the bulk behavior.

High-resolution X-ray microcomputed tomography (XCT) enables for the 3D observation

of cracks in optically opaque materials such as metals and alloys. To measure 3D displacement fields near crack fronts in loaded specimens, two distinct approaches are employed based on tomography images, namely, 3D particle tracking (PT) [8] and digital volume correlation (DVC) [9]. The PT method involves tracking the motions of individual microstructural markers within the material. It is suitable for cases where the images contain discrete features against a homogeneous background (*e.g.*, precipitates within a metallic alloy). Qu et al. [10] measured the local crack driving forces in an aluminum alloy fatigue crack, which provided valuable insights into the crack behavior. Toda et al. [11] quantified the *J*-integral and driving force during an in situ tensile fracture test on an aluminum alloy by tracking porosities. Yang et al. [12] performed thermal imaging tests combined with PT to quantify the temporal and spatial changes of water-heat migration both inside and outside rock fractures. Different from PT, DVC focuses on correlating the gray level contrast between reference and deformed volumes. It has proven to be effective in estimating CODs and SIFs. Furthermore, the measurement uncertainty level of DVC has been demonstrated to be smaller than that of PT [13]. Réthoré et al. [14] analyzed three-dimensional fatigue crack propagation in the cross-section of a pre-cracked cast iron sample while evaluating SIFs along crack fronts using eXtended DVC. Lachambre et al. [15] monitored the growth of a fatigue crack inside a nodular cast iron and computed SIFs along the curved front. Valle et al. [16] developed Heaviside based DVC to assess the local COD and SIF under mode I loading conditions in a fractured polymer sample. Jin et al. [17-18], Shen et al. [19], and Chen et al. [20] quantified 3D crack propagation of fine-grained nuclear graphite under different loading modes using DVC and finite element analyses. Koko et al. [21] characterized the 3D fatigue crack fields of nodular graphite cast iron by combining DVC and finite element simulations. The position of the crack front was determined with three independent techniques and the SIFs were assessed with interaction integrals.

Although DVC is feasible in quantifying damage growth, it still suffers from a big challenge, namely, ill-posedness [22]. An unavoidable compromise between the measurement uncertainty and the spatial resolution has to be found. A global approach to DVC [23] may overcome this limitation, which generally assumes continuous displacement fields. A straightforward connection between experiments and simulations is obtained when considering the same FE mesh [24, 25]. However, due to noise sensitivity and limited available information

(*i.e.*, intensity levels) within a small spatial resolution (*e.g.*, voxel scale), additional regularization techniques (*e.g.*, Tikhonov regularization [26], mechanical regularization [27]) are still desirable to further circumvent the ill-posedness of registration. Moreover, a brittle damage law [28] and node splitting [29] may be used to capture displacement discontinuities across cracked surfaces. A mesh refinement scheme [30] may also be useful to describe the complex behavior of cracks, especially for the crack surface and its front. Such DVC scheme has demonstrated its efficacy to quantify damage in brittle materials including coal [30] and sandstone [31].

In many cases, the evaluation of 3D displacement fields near the cracked surface has been limited to small cracks, typically with CODs less than 4 voxels (abbreviated as vx hereafter) [14]. The mesh size in the vicinity of the crack front is generally larger than 8 vx [15]. Yet a precise estimation of COD and SIF relies on accurate descriptions of the crack surface. Thus, voxel-scale resolutions are essential for capturing the details of the crack opening behavior. Furthermore, the whole process of gradually cracking from small to large cracks (*i.e.*, COD $>$ 10 vx) is also of significance to understand the fracture behavior. Therefore, it is crucial to further improve DVC techniques to handle both small and large crack openings for a better description of crack propagation.

In this study, a voxel-scale digital volume correlation (DVC) approach utilizing 8-noded cube elements is employed to quantify the 3D crack propagation and key parameters (*i.e.*, displacement and strain fields, CODs, and SIFs) of a nodular graphite cast iron under tensile (in situ) loading. The aim is to show that the DVC framework enabled very large CODs to be measured. The first part introduces the material, in-situ experimental setup, and reconstructed volumes to provide an initial understanding of the 3D crack shape. The next section describes advanced DVC and SIF extraction algorithms. A performance assessment is first conducted using a virtual Mode-I crack case. Last, DVC results of the real test case are presented and discussed.

2. Material and experiment

2. 1 Material

This study focuses on the analysis of a ferritic cast iron specimen. The composition of the material consists of 3.4 wt.% C, 2.6 wt.% Si, 0.05 wt.% Mg, 0.19 wt.% Mn, 0.005 wt.% S and 0.01 wt.% P. The ferritic matrix was obtained through casting and subsequent heat treatment, involving ferritization at 880°C followed by air cooling. The volume fraction of graphite nodules was approximately 14%. The carbon and iron matrix exhibit significant differences in X-ray attenuation, thereby resulting in high contrast for DVC registration purposes [13]. The material properties include a Young's modulus of 175 GPa, a yield stress of 315 MPa, and a Poisson's ratio of 0.27 [13]. These properties correspond to the macroscopic response of the material with no distinction between the ferritic matrix and the graphite nodules. A horizontal pre-crack was introduced through fatigue loading on a larger specimen, from which the analyzed sample was subsequently extracted.

2. 2 In situ tensile test

A region of interest (ROI) of 220×270×940 vx^3 (*i.e.*, 1.4×1.7×5.9 mm^3) was imaged using the micro-CT scanner (North Star Imaging X50+) of LMPS with a voxel resolution of 7.3 μm. A total of nine tomographic scans was acquired at different stages of tensile loading. The displacement was kept constant during each scan. The reconstructed volumes are denoted as V_0, V_1, V_2, V_3, V_4, V_5, V_6, V_7, and V_8, as depicted in Fig. 1. The initial four scans (V_0, V_1, V_2, and V_3) revealed minimal crack reopening, which refers to precrack reopening under the influence of a new tensile load. In contrast, scans V_4, V_5, and V_6 highlighted more crack openings and propagation. Last, scans V_7 and V_8 indicated ductile fracture with significantly larger crack openings associated with ductile tearing. It is worth noting that with the selected testing machine, the sample is not visible when mounted.

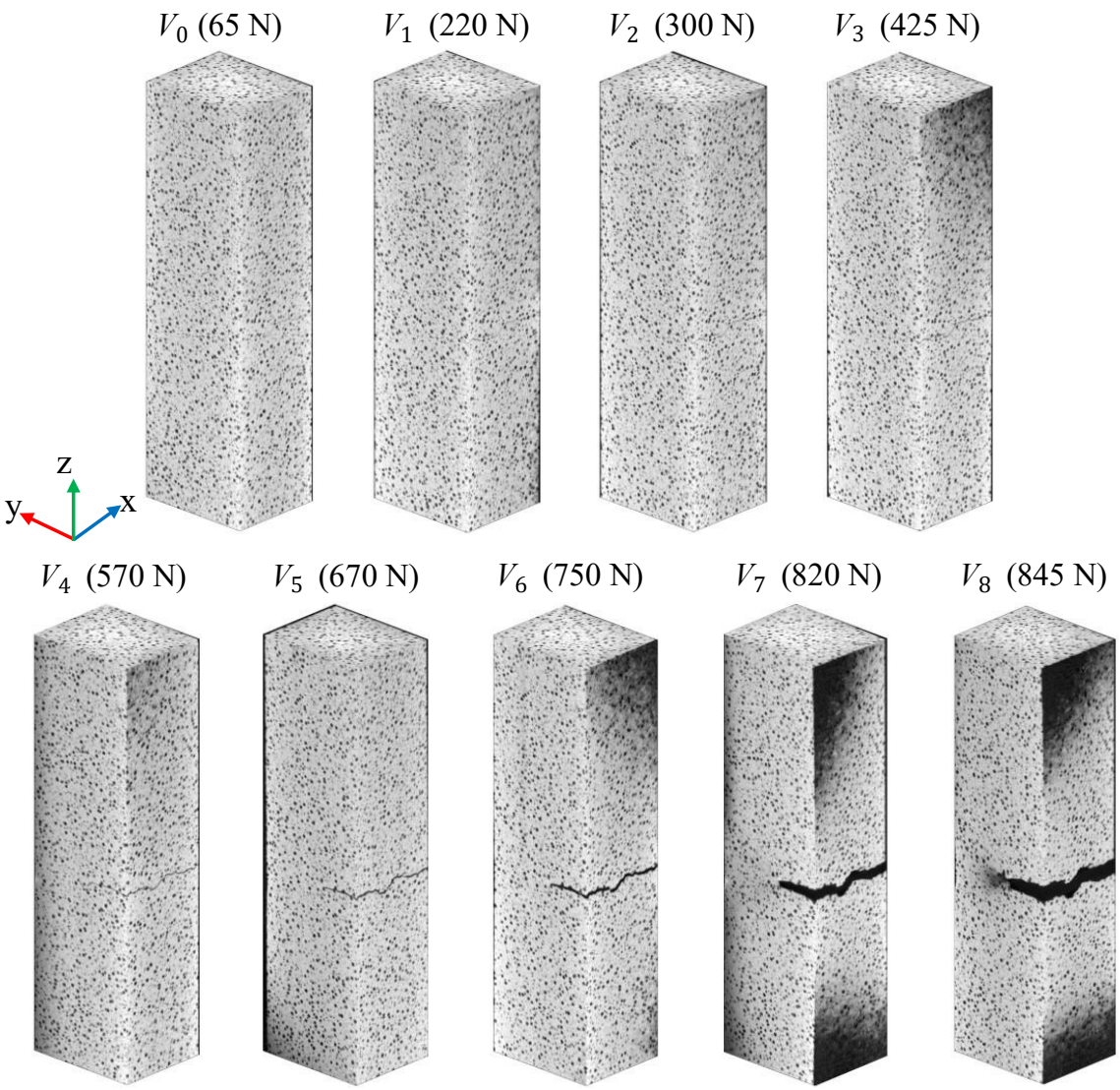

Fig. 1 3D rendered volumes for different scans for increasing applied displacements (the corresponding forces are indicated in parentheses)

Table 1. DVC hardware parameters

Tomograph	North Star Imaging X50+
X-ray source	XRayWorX XWT-240-CT
Target/Anode	W
Filter	none
Voltage	140 kV
Current	80 μA
Tube to detector	473.5 mm
Tube to object	20.0 mm
Detector	Dexela 2923
Definition	1536 × 1944 pixels
Number of projections	1000
Angular amplitude	360°
Frame average	3
Frame rate	11 fps
Acquisition duration	25 min
Reconstruction algorithm	filtered back-projection
Gray levels amplitude	8 bits
Volume size	220 × 270 × 940 voxels (after crop)
Field of view	1.6 × 2.0 × 6.9 mm^3 (after crop)
Image scale	7.4 μm/voxel

3. Methods

3.1 Digital volume correlation

In global DVC, the displacement fields $\mathrm{u}(\mathrm{x},\{v\})$ between the reference volume V_0 and deformed volume V_n is measured by minimizing the *L2*-norm of the gray level residuals [32]

$$\Phi_c^2 = \sum_{\mathrm{ROI}}[V_0(\mathbf{x}) - V_n(\mathbf{x}+\mathbf{u}(\mathbf{x},\{\boldsymbol{v}\}))]^2 \quad (1)$$

Where the sought displacement field $\mathbf{u}(\mathbf{x},\{\boldsymbol{v}\})$ is parameterized in an FE sense (*e.g.*, 8-noded cube elements)

$$\mathbf{u}(\mathbf{x},\{\boldsymbol{\upsilon}\}) = \sum_i \upsilon_i \boldsymbol{\phi}_i(\mathbf{x}) \quad (2)$$

for which $\boldsymbol{\phi}_i(\mathbf{x})$ is the shape function associated with the degrees of freedom υ_i. A Gauss Newton iterative procedure is then applied, leading to linear systems [33]. Mechanical regularization related to the local equilibrium gap [34] is further considered to render the solution less affected by acquisition noise and reconstruction artifacts

$$\Phi_m^2 = \{\mathrm{d}\boldsymbol{\upsilon}\}^{\mathrm{T}}[\mathbf{K}_{\boldsymbol{m}}]^{\mathrm{T}}[\mathbf{K}_{\boldsymbol{m}}]\{\mathrm{d}\boldsymbol{\upsilon}\} \quad (3)$$

where $[\mathbf{K}_{\boldsymbol{m}}]$ is the rectangular stiffness matrix of the regularized nodes, and $\{\mathrm{d}\mathbf{u}\}$ the displacement increment between two analyzed volumes. Such regularization is based on the assumption of Hencky elasticity at the local level [35], which is beneficial to prevent over-filtering, especially in plastic regions. Therefore, the total cost function reads

$$\Phi_t^2 = \Phi_c^2 + \omega_m \Phi_m^2 \quad (4)$$

The weight ω_m is proportional to a length ℓ_{reg} raised to the power 4 [36], namely, the so-called regularization length. In addition, a master-slave [37] regularization was used to mitigate displacement fluctuations on the Dirichlet boundaries. In such DVC scheme, the spatial resolution can be lowered to the voxel-scale [38]. The damaged elements traversed by the cracked surface are removed to capture a large-scale crack opening. More details on such schemes are found in Ref. [30].

3.2 Stress intensity factor extraction

In 2D analyses [39], Williams' series [40] have been employed to determine SIFs for nearly straight crack paths [41, 42]. However, there have been limited applications in the 3D context. Notably, Limodin et al. [43] and Lachambre et al. [15] calculated SIFs by performing least-squares projection of displacement fields measured via DVC. In this study, SIFs are determined from displacement fields obtained through an advanced DVC approach. Initially, the implementation is presented using a virtual cracking test case, and then it applied to an in situ tensile test conducted on nodular graphite cast iron.

3.2.1 Williams' series

It is assumed that each nodal layer orthogonal to the mean direction of the crack front can be treated separately. For each nodal layer, the reference 3D displacement field reads

$$\mathbf{u}(r,\theta) = \sum_{j=I}^{III} \sum_{n=p_i}^{p_n} \omega_n^j \, \boldsymbol{\Psi}_n^j(r,\theta) \quad (5)$$

where the vector fields are defined in the polar coordinate system (r, θ) centered about the crack front position, ω_n^j the amplitudes to be determined, n the index of Williams' series (in this work, n = -1, 0, …,7), and $j = I$ is related to the mode I (opening) regime

$$\boldsymbol{\Psi}_n^I = \frac{r^{n/2}}{2\mu\sqrt{2\pi}}\left[\kappa\exp(i\frac{n}{2}\theta) - \frac{n}{2}\exp\left(2i\theta - i\frac{n}{2}\theta\right) + \left\{(-1)^n + \frac{n}{2}\right)\exp(-i\frac{n}{2}\theta\right\}\right] \quad (6)$$

$j = II$ to mode II (in-plane shear)

$$\boldsymbol{\Psi}_n^{II} = \frac{ir^{n/2}}{2\mu\sqrt{2\pi}}\left[\kappa\exp(i\frac{n}{2}\theta) + \frac{n}{2}\exp\left(2i\theta - i\frac{n}{2}\theta\right) - \left\{(-1)^{n+1} + \frac{n}{2}\right)\exp(-i\frac{n}{2}\theta\right\}\right] \quad (7)$$

$j = III$ to mode III (tearing)

$$\boldsymbol{\Psi}_n^{III} = \frac{r^{n/2}}{2\mu\sqrt{2\pi}}\cos(\frac{n(\theta-\pi)}{2}) \quad (8)$$

with κ = 3 - 4ν for plane strain conditions, and ν the Poisson's ratio. The amplitudes ω_0^j give access to the rigid body translations, amplitudes ω_1^j to SIFs, ω_2^I and ω_2^{III} provide the T-stress, ω_2^{II} offers one rigid body rotation. Higher-order (sub-singular) fields explain deviations from the assumption of infinite medium theory [44]. In addition, the first mode I super-singular field (n = -1) enables the crack front position to be determined by canceling out the corresponding amplitude [41]. Assuming that there is a small offset d of the crack front position along the propagation path, it is expressed as [45]

$$d = \frac{2\omega_{-1}^I}{\omega_1^I} \quad (9)$$

3.2.2 Displacement projection

Considering a cracked surface with a roughly estimated crack front (Fig. 2), DVC measured displacements are projected onto Williams' series over circular domains (*i.e.*, pacman planes). The Williams' matrix $[\mathbf{S}_{\boldsymbol{\omega}}]$ collecting all unitary fields $\boldsymbol{\Psi}_n^j$ for each pacman plane is constructed, and the least squares minimization leads to a linear system

$$[\mathbf{S}_{\boldsymbol{\omega}}]\{\boldsymbol{\omega}\} = \{\mathbf{u_p}\} \quad (10)$$

in which $\{\boldsymbol{\omega}\}$ gathers all unknown amplitudes of Williams' series, and $\{\mathbf{u_p}\}$ the column vector of measured nodal displacements. A least squares step is run to estimate all unknown amplitudes, and a new crack front position is estimated by using the update to the crack offset. The previous step is repeated until all the absolute values of the shift d are all less than one voxel. Last, the corresponding SIFs are extracted from the converged solution.

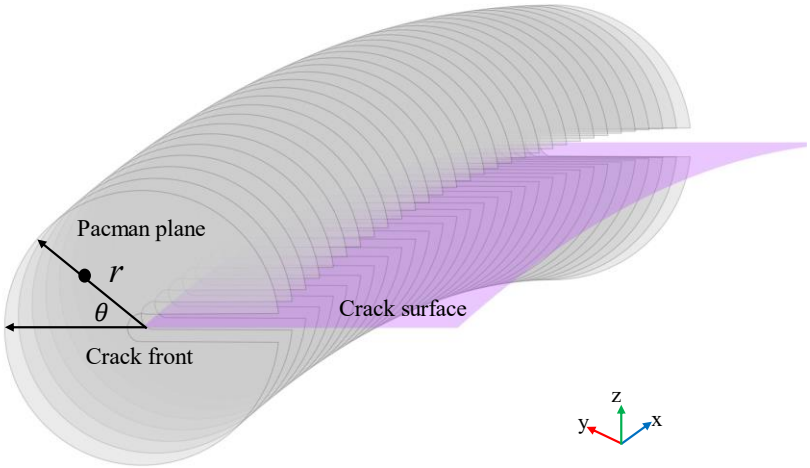

Fig. 2 Schematic 3D rendering of 2D pacman planes centered about the crack front used for the projection of the displacement onto Williams' series. The black arrows define the crack frame in polar coordinate systems (r, θ) and the purple plane highlights the cracked surface.

4. Results and discussions

4.1 Virtual crack testing case

4.1.1 Generating cracked volume

A virtual crack testing case is presented to assess the performance of voxel-scale DVC. Figure 3 illustrates the process for generating deformed volumes, which involves the following steps:

1) Consider a reference volume $V_0(\mathbf{x_v})$ (Fig. 3(a)) whose size is $210 \times 210 \times 350$ vx^3 extracted from the original scan V_0, in which $\mathbf{x_v}$ are integer-valued voxel positions;
2) A voxel-wise displacement field $\mathbf{u}(\mathbf{x_v})$ (Fig. 3(b)) is calculated according to the pure mode I crack solution in Williams' series with a sloping straight crack front;
3) Find non-integer positions $\mathbf{x_0}$ in V_0 corresponding to integer positions $\bar{\mathbf{x}}_\mathbf{v}$ in the deformed volume $V(\bar{\mathbf{x}}_\mathbf{v})$ based on the inverse deformation mapping $\mathbf{x_0} = \boldsymbol{\beta}^{-1}(\bar{\mathbf{x}}_\mathbf{v})$, in which $\boldsymbol{\beta}(\mathbf{x_0}) = \mathbf{x_0} + \mathbf{u}(\mathbf{x_0}) = \bar{\mathbf{x}}_\mathbf{v}$. In the present implementation, a Newton iterative scheme was used to determine $\mathbf{x_0}$;
4) Generate $V(\bar{\mathbf{x}}_\mathbf{v}) = V_0(\mathbf{x_0})$ (Fig. 3(c)) using spline interpolation of the gray levels. A flat crack surface is observed in the middle of the z-direction with a straight crack front (in blue). Last, Gaussian white noise is added with a standard deviation of 10 gray levels (*i.e.*,

5% of the dynamic range) to simulate acquisition noise and reconstruction artifacts. Such noise level was estimated from the standard deviation of gray level residuals between the first two scans (*i.e.*, scans V_0 and V_1), which is rather high in order to be challenging.

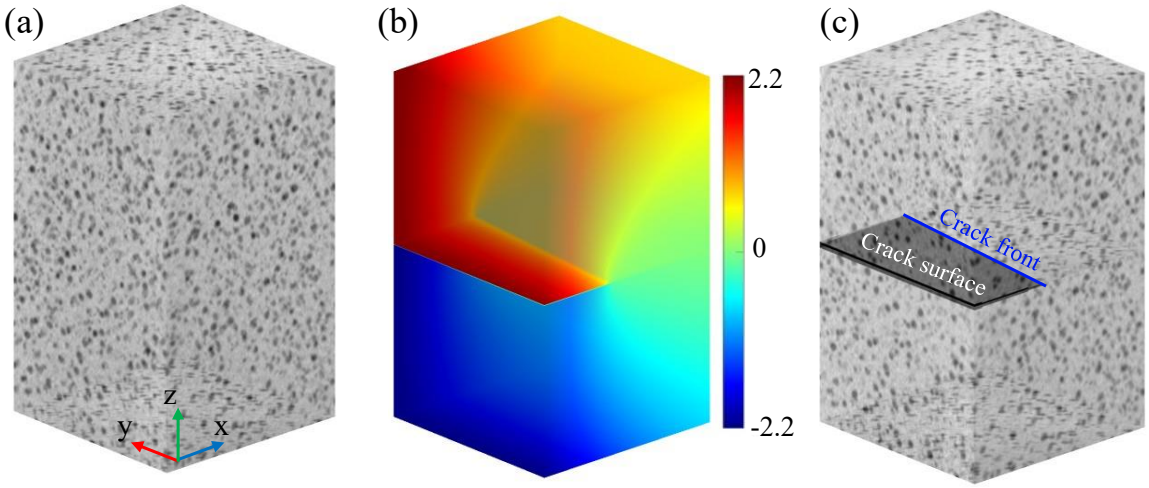

Fig. 3 Schematic views of generating a virtually cracked volume. (a) Reference volume. (b) Voxel-wise displacement field u_z. (c) Deformed volume for which white Gaussian noise was added.

4.1.2 Voxel-scale DVC results

The registration between the above reference and deformed volumes was performed with advanced DVC. An adaptive pyramidal mesh (*i.e.*, ℓ = 24-8-4-2 vx) was used to account for voxel-scale damage while ensuring computational efficiency. The regularization length and the master/slave boundary regularization mesh size are equal to 80 vx and 48 vx, respectively. Figure 4(a) displays the measured displacement field u_z with the overlaid multiscale mesh. The prescribed (Fig. 3(b)) and measured (Fig. 4(a)) displacement fields show strong agreement, thereby indicating that the proposed DVC framework can efficiently capture displacement discontinuities with voxel-scale meshes around the cracked surface. Furthermore, the histogram of nodal displacement residuals (defined as the difference between measured and prescribed quantities) is reported in Fig. 4(b) to assess measurement errors. The presence of a Gaussian-like distribution within the range of -0.1 to 0.1 vx indicates high quality performance even in such challenging condition. Higher displacement residuals are mainly observed at the boundary and near the crack front due to the limitations of the master-slave and mechanical

regularizations. Conversely, lower displacement residuals are likely attributed to acquisition noise and interpolation errors in both displacement and gray levels.

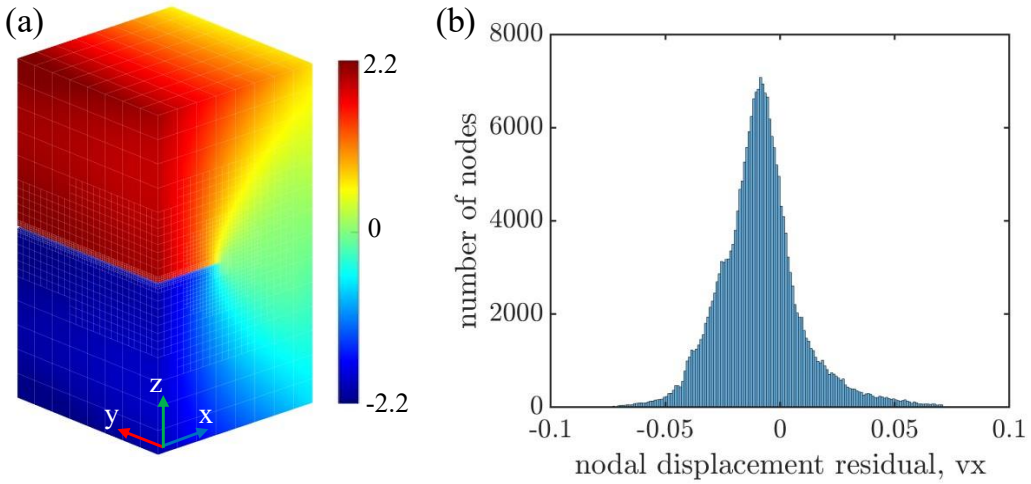

Fig. 4 (a) Measured displacement field u_z expressed in voxels. (b) Histogram of nodal displacement residuals.

4.1.3 SIFs extraction results

The crack front and SIF were determined using the procedure outlined in Section 3.2. In the lower-left corner of Fig. 5(a), a pacman-like mesh is displayed along the crack front. Here, the mesh size in the *xOz* plane ranged from coarse (6 vx) to fine (3 vx), while the mesh size along the *y*-direction was set to 6 vx. The removed inner and outer circles have a radius of 10 vx and 150 vx, respectively. As observed in Fig. 5(a), both measured crack fronts obtained via DVC gray level residuals (*i.e.*, crack defined as gray level residuals exceed the noise level threshold of 10 GL) and Williams' series were in strong agreement with the prescribed one. The corresponding absolute errors in the measurement of the crack front along the sample thickness are almost within 1 vx. The estimated mode I SIF K_I (left *y*-axis in Fig. 5(b)) follows an identical trend with the exact solution but exhibits a slight decrease, possibly due to the influence of enforced elastic regularization. Despite this decrease, the relative error (Fig. 5 (b)) remains within the range of 1% to 1.5%, indicating a good performance of the proposed identification scheme.

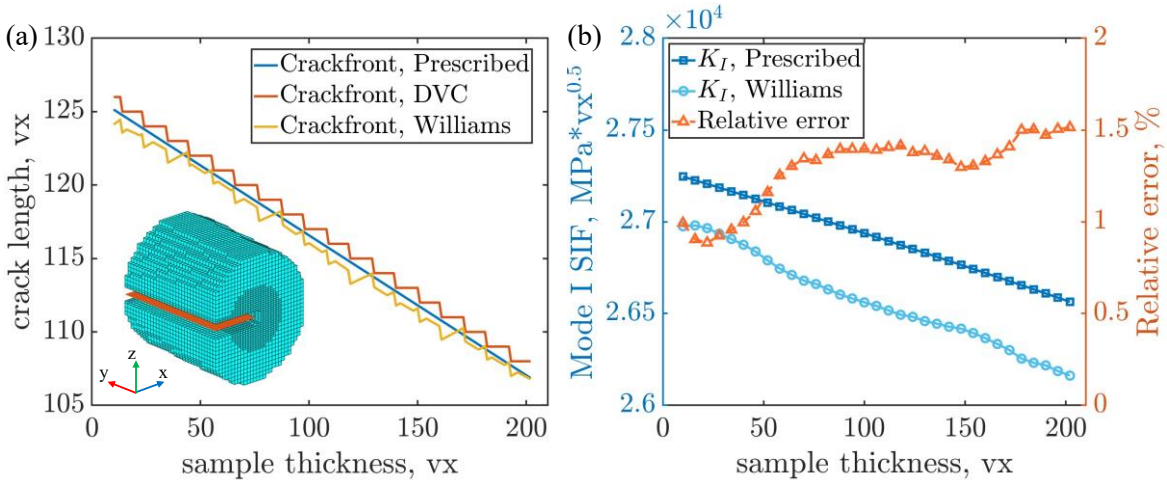

Fig. 5 (a) Crack front determined by different methods. The used pacman-like mesh is shown in the lower-left corner. (b) Identified mode I SIF and corresponding relative error.

5. DVC results and discussions of an in-situ tensile test

5. 1 Standard uncertainty

A cubic ROI with a size of 200×200×200 vx^3 extracted from the reference volume (*i.e.*, scan V_0) was used to evaluate the standard measurement uncertainty of the proposed DVC framework. The equivalent speckle size, determined by autocorrelation [46] was found to be 2.4 vx. The root-mean-square (RMS) image gradients along the three directions, denoted as RMS(∇f_x) = 13.1, RMS(∇f_y) = 12.4, and RMS(∇f_z) = 12.3 GL/vx, respectively, indicated that the image contrast was almost identical along the three directions. To assess the standard displacement and maximum principal strain (*i.e.*, the strain tensor within one element is solved by finite difference of nodal displacements) uncertainties, white Gaussian noise with a standard deviation of 10 gray levels was added. The standard deviations of displacement and maximum principal strain were approximately 0.1 vx and 0.001, respectively, as shown in Fig. 6. Without regularization, increasing the mesh size resulted in reduced standard uncertainty because more voxels were used to evaluate each nodal displacement.

Introducing regularization significantly reduced the standard uncertainty for a given mesh size following a power law trend observed in all three fitted curves. This regularization allowed for measuring displacements at very small spatial resolutions (*e.g.*, 10 voxels in this study) while maintaining low uncertainty. However, excessive regularization may lead to over-smoothing, since elasticity is enforced in areas where it is not applicable, such as in the cracked

zone. Consequently, a compromise between mechanical regularization and image correlation residuals has to be found for each scan.

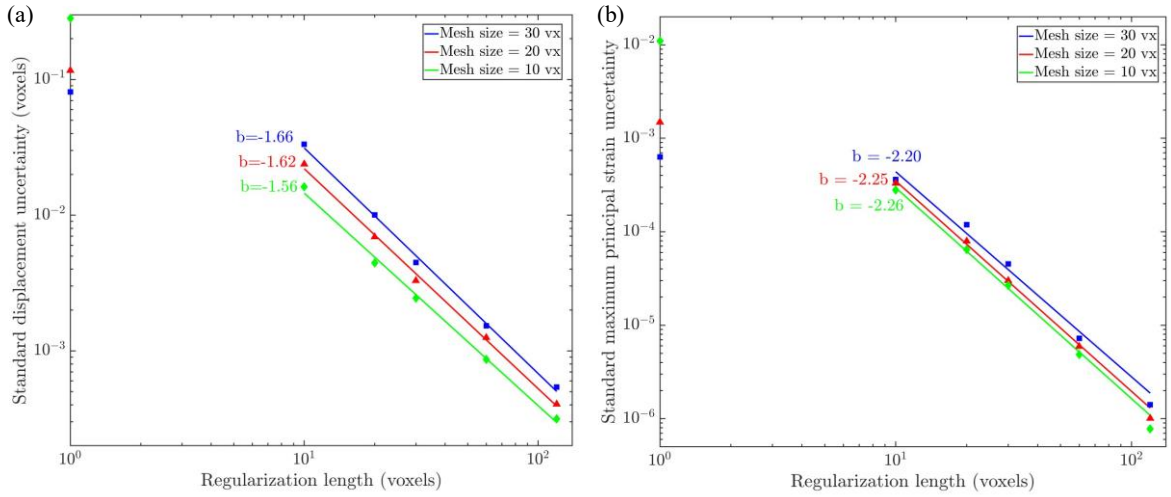

Fig. 6 Standard measurement uncertainties as functions of regularization length for (a) nodal displacements and (b) maximum principal strain

5. 2 Mesoscale damage analyses

A mesh with split nodes on the whole ROI was produced (Fig. 7 (a)) to account for the discontinuity of the cracked region in a rough way. The measured residual curves (*i.e.*, mechanical residual ρ_{mec} vs. normalized correlation residual ρ_{dvc}) [38] (Fig. 7 (b)) enabled for the selection of an appropriate regularization length, which corresponds to the inflection point of each curve [47]. A consistent linear trend was observed in scans V_1 to V_4, indicating predominantly elastic deformation. As a result, a larger regularization length of 80 vx was chosen as a low-pass filter, resulting in standard displacement and maximum principal strain uncertainties of 5×10^{-4} vx and 3×10^{-6}, respectively. Conversely, a gradual bending over trend occurred for scans V_5 to V_8, indicating the presence of plasticity and damage. Consequently, a lower regularization length of 40 vx was selected. With this choice, the corresponding displacement and strain uncertainties were measured at 2×10^{-3} vx and 2×10^{-5}, respectively.

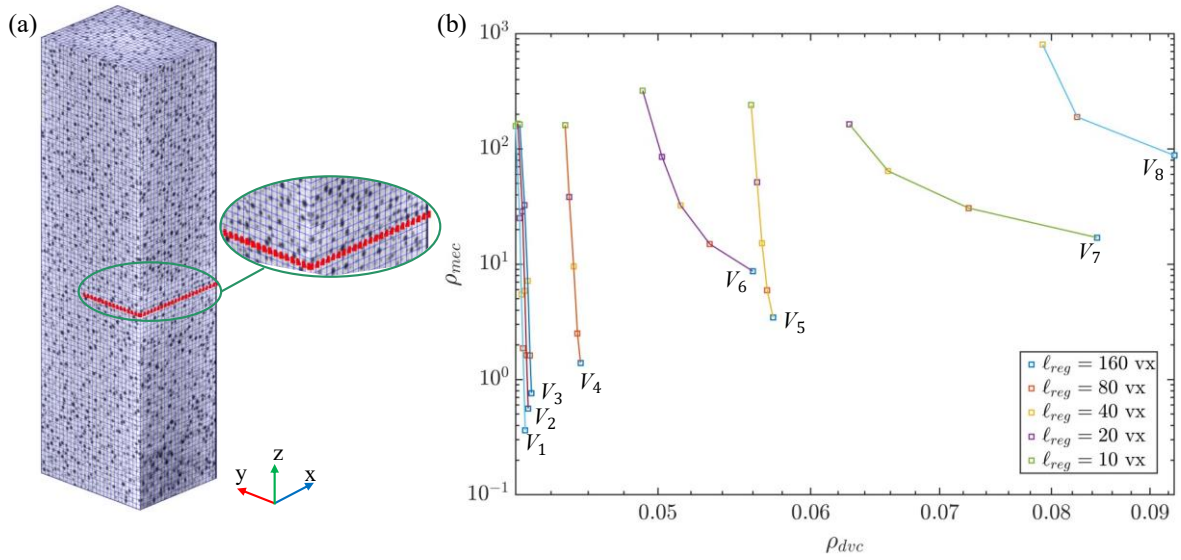

Fig. 7 (a) DVC mesh with split nodes (in red) laid over the reference rendering volume. The mesh size is equal to 10 vx. (b) Mechanical vs. DVC residuals for different regularization lengths.

The thresholded gray level residual fields (Fig. 8) for the different scans reveal distinct characteristics of the crack. Each scan exhibits two vertically distributed bands due to imperfect volume reconstruction. Furthermore, regions with high residuals indicate the presence of the crack, enabling for the visualization of its shape and propagation. Notably, the crack surface appears to be nearly horizontal and progressively propagated inward with the applied loading. Three stages of crack development are distinguished. First, crack reopening before scan V_4 because all gray level residuals are in an similar range, indicating that the crack opening scale is below the CT resolution. Second, from scans V_4 to V_5, there is noticeable crack opening with limited propagation. The thresholded residuals clearly reveal the presence of the cracked surface. Last, macroscopic ductile tearing occurred in scans V_6 to V_8. The cumulated thresholded residual points gradually thicken the crack surface, thereby indicating that such DVC calculations near the crack front was not trustworthy.

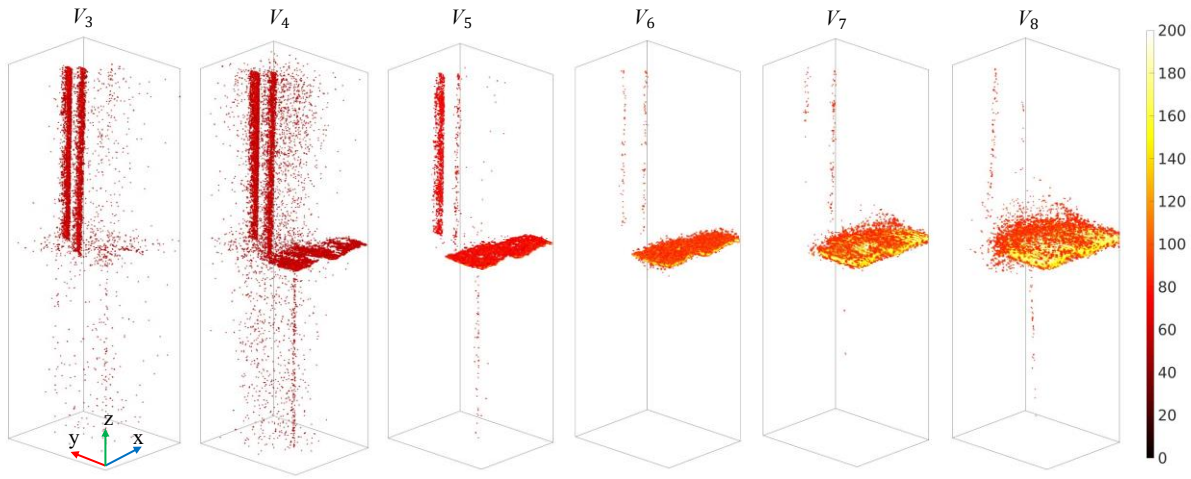

Fig. 8 Thresholded gray level residual fields (unit: GL) for different stages of loading. Threshold = 50 gray levels for scans V_3, V_4, and V_5, or 80 GL for scans V_6, V_7, and V_8.

5.3 Voxel-scale damage analysis

5.3.1 Crack growth updating strategy

To investigate the crack development at the voxel-scale, a crack growth updating strategy based on advanced DVC was performed on a small ROI containing the crack, as shown in Fig. 9. There are two cycles in the whole process, namely, the first cycle for crack quantification for the current scan (orange arrow in Fig. 9(a-d)), and the second cycle for crack identification in the next scan (blue arrow in Fig. 9(e-g)). The proposed methodology consists of the following steps:

1) The reference volume V_0 and the deformed one V_n (*i.e.*, the *n-th* scan, here $n = 4$) are taken as initial input to estimate the crack path with the registration residuals (Fig. 9(a)), which are extracted from the thresholded gray level residual field (*i.e.*, scan V_4 in Fig. 8);

2) The corresponding crack surface (Fig. 9(b)) is fitted based on the residual points. A coarse-graining approach is used (Fig. 10(a-d)) in which the residual points far from the fitted surface are removed in each fitting step to suppress outliers. The crack front is estimated by fitting and eventually checked by the uncertainty of CODs;

3) An adaptive multiscale mesh (*i.e.*, ℓ = 24-8-4-2 vx) for advanced DVC calculations is generated based on the fitted crack surface (Fig. 9(c)). The damaged elements are removed to describe discontinuity. The voxel-scale mesh (*i.e.*, 2 vx) surrounding the crack surface allows for a precise description of the crack morphology. The master mesh size for boundary regularization is equal to 48 vx;

4) Advanced DVC is run to calculate the deformation fields (Fig. 9(d)) for the current scan, including displacement and strain fields;

5) The mesh in step 3 is directly used in the next scan (*i.e.*, V_{n+1}, Fig. 9(e)) owing to the continuity of crack growth to estimate the corresponding thresholded gray level residual field (Fig. 9(f));

6) Keep the previous fitted crack surface and find the nascent residual points (in green) near the new crack front (Fig. 9(g)). A new map is then recreated by considering all points of Fig. 9(g);

7) The 6 steps are repeated until all scans are studied.

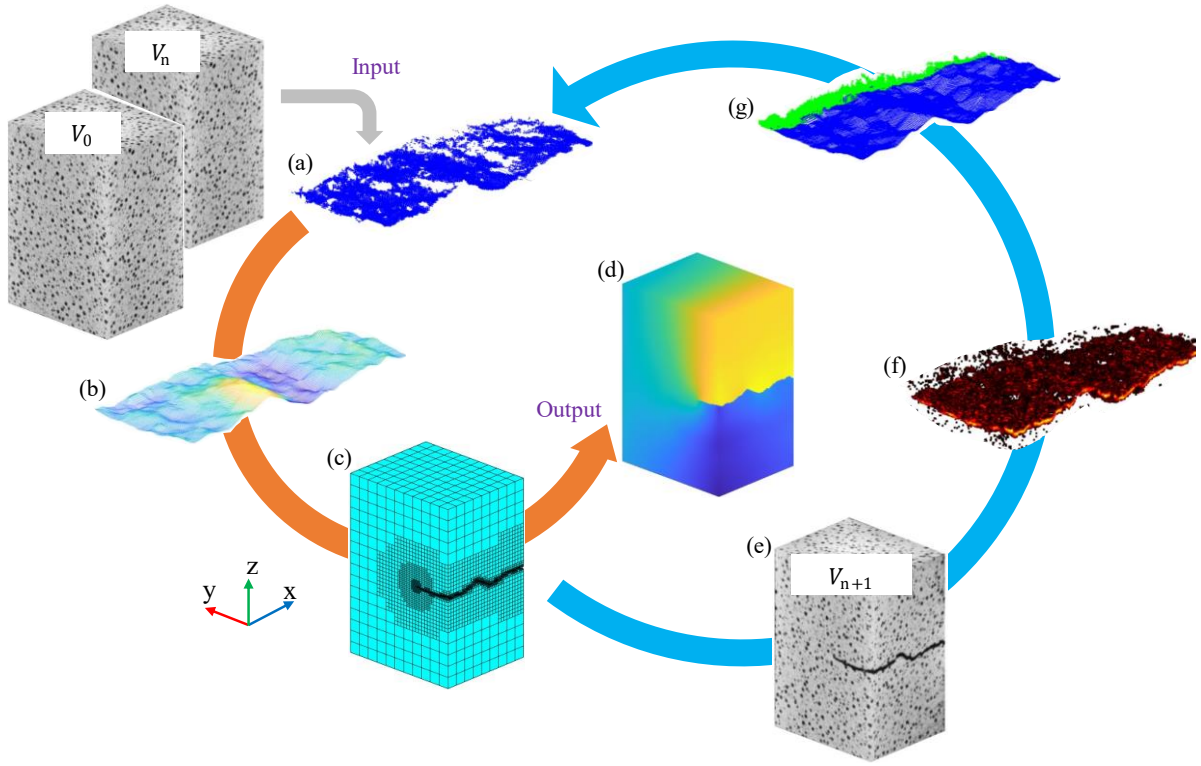

Fig. 9 Flowchart of the crack growth updating strategy. (a) Gray level residuals for the current scan. (b) Fitted crack surface. (c) Adaptive multimesh DVC. (d) Deformation fields for the current scan. (e) Deformed volume (next scan). (f) Gray level residuals for the next scan. (g) All points of the crack surface fitting of the next scan.

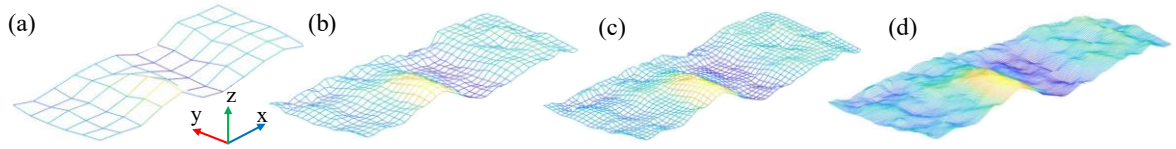

Fig. 10 Example of crack surface fitting process for decreasing mesh sizes (unit: vx). (a) 24×18, (b) 8×6, (c) 4×3, (d) 1×1 resolutions.

5.3.2 3D crack shape and propagation

From the above-mentioned procedure, the 3D growing crack surface in each scan was determined based on the gray level residual fields. Furthermore, considering the uncertainty of COD, particularly near the crack front, allowed for the characterization of the 3D crack shape and its propagation as illustrated in Fig. 11(a). The crack exhibits a tendency to bypass or traverse the graphite nodules, thereby resulting in a wavy crack surface. In the early loading stages (scans V_1 to V_3), the crack reopened slightly with a very small COD below the CT resolution. In the medium loading stage (scans V_4 to V_5), the crack front penetrated deeper into the sample leading to more crack opening (above the CT resolution). However, there was only a small and stable growth of the crack front observed between scans V_4 and V_5. In the final loading stages (from scans V_6 to V_8), the crack front experienced significant inward propagation, accompanied by changes in the 3D crack shape. These findings provide insights into the progressive behavior of the crack under (re)loading conditions.

The positions of the crack front along the sample thickness for different scans quantitatively reveal the crack shape and its propagation (Fig.11(b)). The crack front shape had large fluctuations in scans V_1 and V_2 with a mean crack length of approximately 200 μm (or 30 vx). For scan V_3, the crack front exhibited an inclined profile with deeper propagation on the left along the sample thickness than on the right. The mean crack length is approximately 400 μm (or 60 vx), which is much smaller than that in scan V_4 (*i.e.*, 600 μm or 90 vx). A smaller increment of crack length (*i.e.*, 80 μm or 90 vx) is observed between scans V_4 and V_5, which proves that the opening was gradual. In addition, the crack length gradually increased from the left to the right along the sample thickness indicating that crack opening was not uniform. Larger increments in crack length for the last three scans indicate ductile tearing and the crack front shape was almost arch-like due the presence of plasticity.

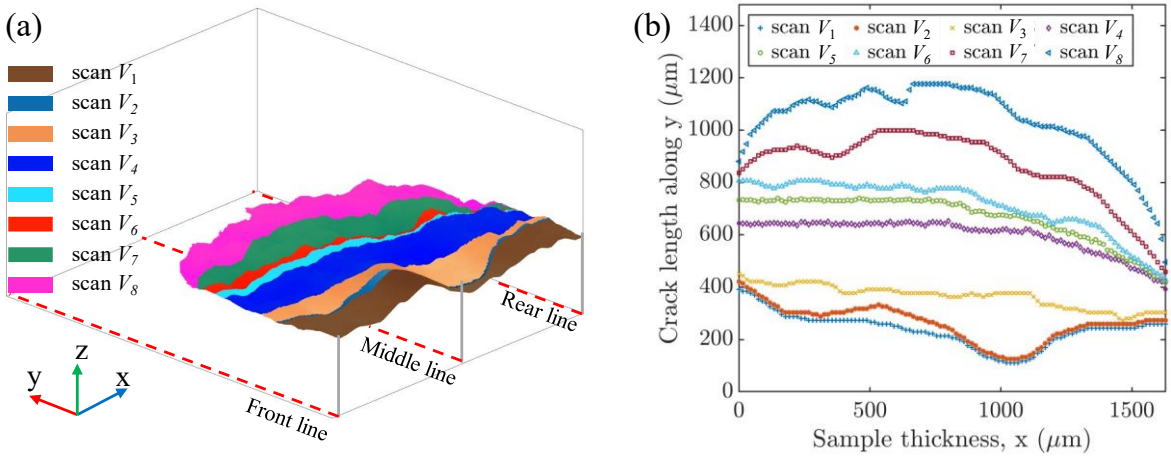

Fig. 11 Crack characteristics for the different scans. (a) 3D renderings of the cracked surface. (b) Corresponding crack front positions along the sample thickness.

5.3.3 Displacement fields in the bulk of the sample

The displacement fields in the reference and deformed configuration of the last scan (V_8) are displayed in Fig. 12, with the top and bottom rows representing each configuration, respectively. The crack introduced a significant and noticeable discontinuity in the u_x and u_z displacement components, which correspond to modes III and I, respectively. This discontinuity enables for the evaluation of crack tearing and opening at a local scale. On the other hand, only minor discontinuities are observed in the mode II (*i.e.*, u_y) displacement field, indicating limited shearing. Furthermore, arc-shaped displacement distributions are observed near the crack front and along the thickness direction of the sample. The displacement jumps in terms of u_x, u_y, and u_z at the crack mouth were approximately 40 μm (or 5.4 vx), 20 μm (or 2.7 vx), and 300 μm (or 41.1 vx), respectively. Significant crack opening and tearing indicate the occurrence of ductile fracture within the bulk of the sample. This fracture resulted in a strong alteration in the geometry before and after deformation.

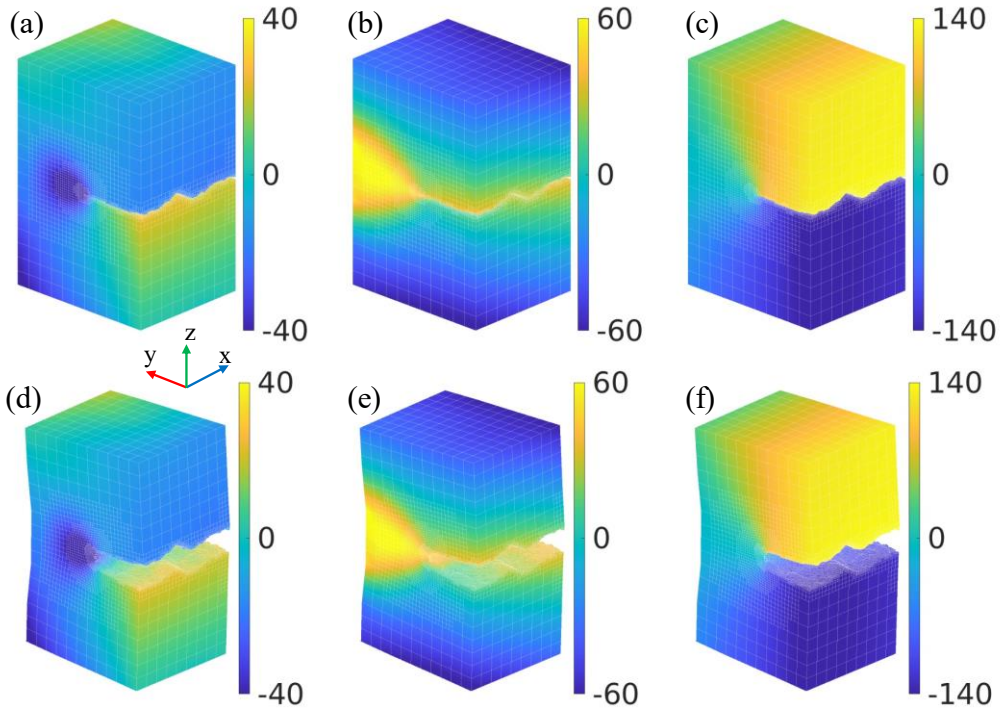

Fig. 12 Bulk displacement fields (unit: μm) in the reference (top row) and deformed (bottom row) configuration of the last scan (V_8). (a,d) u_x, (b,e) u_y, (c,f) u_z components.

5.3.4 Von Mises strain fields in the bulk of the sample

Based on the previous analysis, it was determined that the sample underwent plastic deformation. To assess the shape and size of the plastic zone in different scans, von Mises equivalent strain fields near the crack front were computed. According to a linear constitutive model, the yield strain (ϵ_y) was roughly estimated via Hooke's law given the yield stress (σ_y) and Young's modulus (E) at the macroscopic level (*i.e.*, $\epsilon_y = \sigma_y/\mathrm{E} = 1.8 \times 10^{-3}$). Considering the numerous sources of uncertainty, such as acquisition noise and the presence of complex microstructure and deformation, the plastic zone was defined as the region where the von Mises strain exceeded nine times the standard strain uncertainty or five times the estimated yield strain (*i.e.*, the strain offset was equal to 9×10^{-3}). The crack did not open and propagate significantly before scan V_5. Therefore, it was reasonable to assume the absence of additional plastic deformation from scans V_1 to V_4. With the selected offset strain, the plastic zone remained very small in the first four scans. Figure 13 illustrates the thresholded von Mises strain fields from scans V_5 to V_8. The different viewing angles presented in the top and bottom rows enhance the understanding of the distribution characteristics on the front and rear faces of the sample. Interestingly, the thresholded von Mises strain field was only observed at the

crack front in scan V_4, thereby indicating that the current deformation is still within the elasticity stage. Based on the spatial patterns and variations of the von Mises strain fields, it is observed that the plastic zone gradually increased with the applied loading. Specifically, the average plastic zone radius (*i.e.,* the distance between the crack front and the profile in each *yOz* plane of plastic zone) for scans V_5, V_6, V_7, and V_8 are approximately 300 μm, 450 μm, 660 μm, and 815 μm, respectively. The localized regions with a gradual lighter color surrounding the crack tip are indicative of the areas experiencing significant deformation and plastic flow. In particular, the presence of high strain concentrations in the immediate vicinity of the crack front suggests large deformation and stress concentrations. Furthermore, a roughly symmetrical pattern is observed around the crack tip in all four scans, indicating a nearly aligning tensile loading condition. Slight asymmetry suggests that crack propagation was not uniform, potentially leading to variations in crack growth behavior.

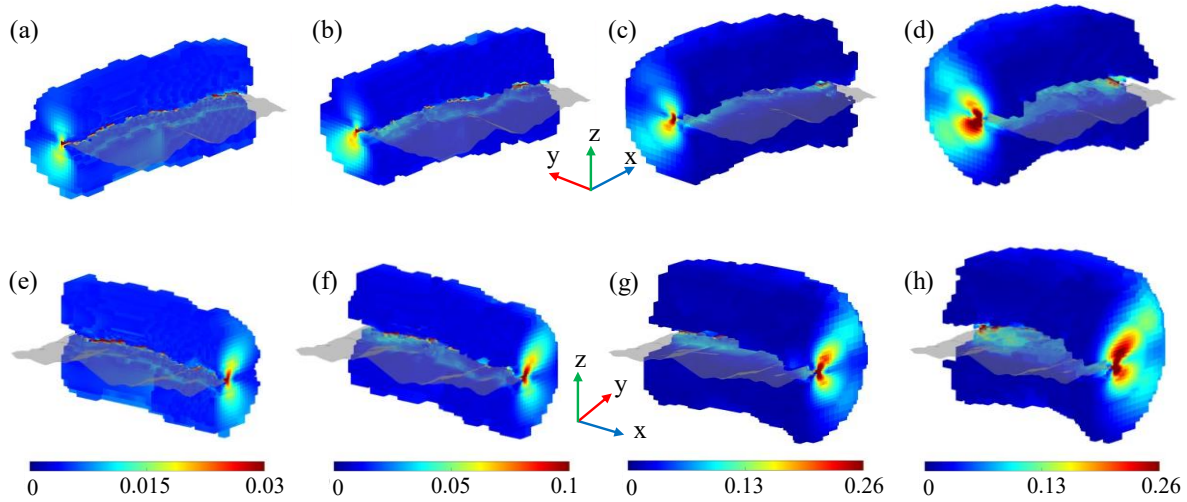

Fig. 13 Thresholded von Mises strain fields under two different viewing angles. (a,e) Scan V_5. (b,f) Scan V_6. (c,g) Scan V_7. (d,h) Scan V_8.

5.3.5 Crack opening displacements

Thanks to voxel-scale measured displacement fields, CODs along three directions (as described in Fig. 18 in Appendix A) for different scans were estimated by calculating the displacement jumps between the upper and lower surfaces of the crack mouth. The norm of these displacement jumps was considered as the average COD (Fig. 14) for which the detection level (*i.e.*, 0.08 vx or 0.60 μm) was defined as 4 times the standard uncertainty based on the first two scans. The COD decayed closer to the crack front. In addition, the COD distribution along the sample thickness (*i.e.*, *x*) direction was not uniform, namely, the COD level on the

front side was higher than at the rear. The range of CODs in the mouth is very large from scans V_1 (*i.e.*, 0.25 vx or 1.85 μm) to V_8 (*i.e.*, 40.0 vx or 296 μm), which shows that the proposed measurement strategy gives quantitative insights into the whole cracking process from crack reopening to final ductile tearing. It is worth noting that CODs at the crack front for scans V_6-V_8 reached several voxels, which is far above the uncertainty level. This observation suggests that the detected crack front may not be sufficiently deep due to the presence of large plastic deformation. Such significant plasticity poses a challenge when fitting the crack front accurately.

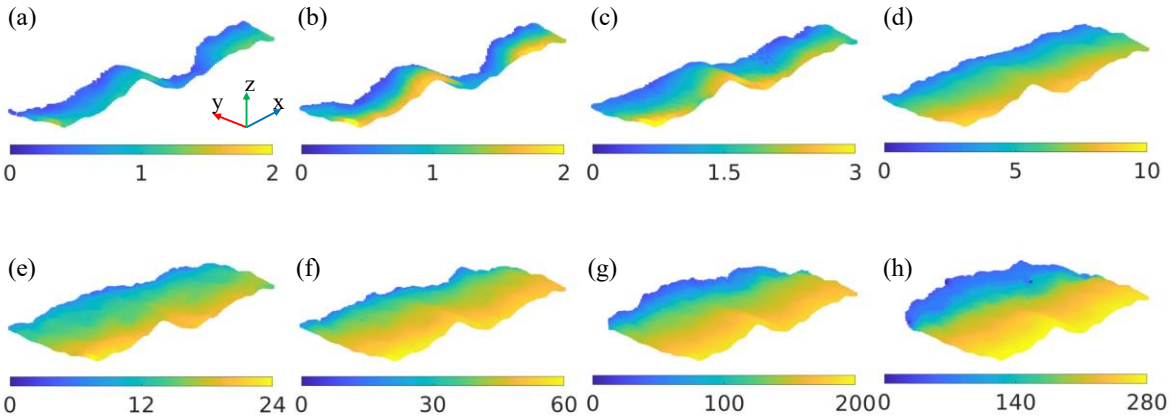

Fig. 14 COD fields (unit: μm) for different scans. (a) V_1, (b) V_2, (c) V_3, (d) V_4, (e) V_5, (f) V_6, (g) V_7 and (h) V_8.

To quantitatively analyze the characteristics of crack propagation, CODs were extracted along three lines (Fig. 11(a)) from the crack mouth to the crack front in scans V_1-V_5. According to Williams' series, the COD amplitudes should be proportional to the square root of the distance to the crack front in its vicinity if linear elasticity applies [48]. The resulting profiles are displayed in Fig. 15, with solid lines representing the best fit curves for each scan, and the dashed line indicating the uncertainty level. The fitted curves closely align with the measured data for all five scans (V_1 to V_5), thereby suggesting that the deformation tends to follow a linear and elastic behavior. The consistent trends observed in the three subfigures indicate similar cracking modes along the sample thickness. However, the varying crack lengths imply non-uniform crack opening throughout the sample thickness. In this particular case, the crack opened faster on the front side, potentially due to slight misalignments of the sample in the testing machine.

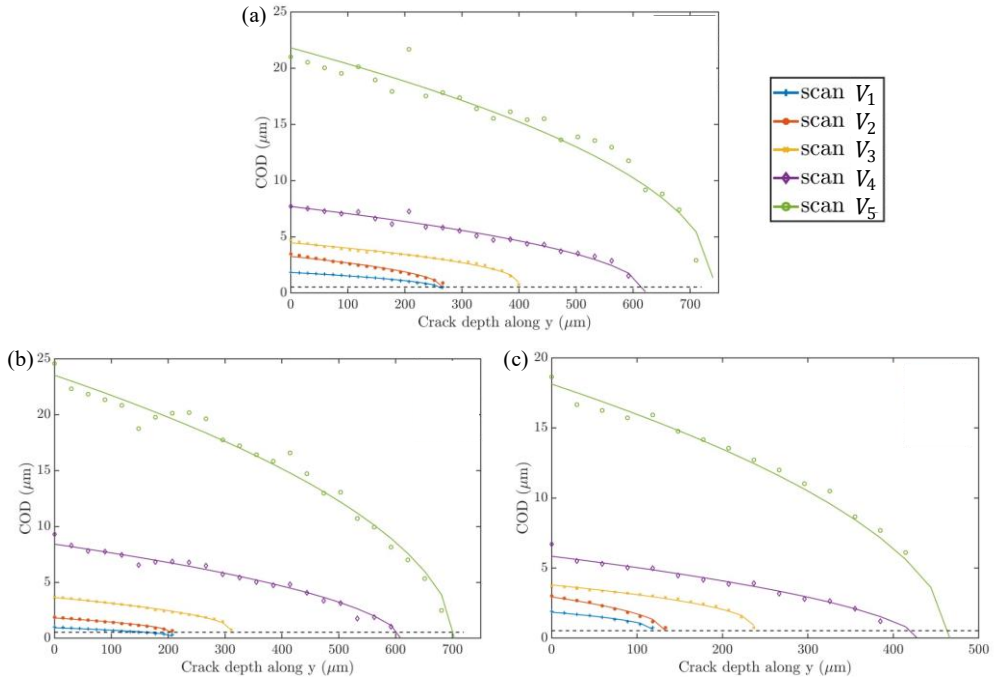

Fig. 15 COD profiles for three different sections. (a) Front line. (b) Middle line. (c) Rear line. The solid and dashed lines represent the best fitting curves and uncertainty level, respectively.

5.3.6 SIFs estimation

To quantify the level of stress intensification at the crack front, the SIFs (*i.e.*, K_I, K_{II}, and K_{III} in Fig. 16) were estimated using the post-processing method from scans V_1 to V_5. The reference volume (*i.e.*, scan V_0) and its deformed state (*i.e.*, corrupted by white Gaussian noise with a standard deviation of 10 GL) were used to evaluate the measurement uncertainty of SIFs. The standard uncertainties of K_I, K_{II}, and K_{III} were 0.4, 0.4 and 0.2 MPa$\sqrt{\text{m}}$, respectively. The mode I SIF K_I shown in Fig. 16(a) is almost identical along the crack front in each scan meaning a symmetric distribution of mode I stress, and it suggests that crack propagation is more likely to occur in a uniform manner. Similar observations were reported for graphite [19]. Sub-voxel crack opening in the first three scans (*i.e.*, V_1 to V_3) were quantified accurately. Small but clear differences are observed among them. For scans V_4 and V_5, the crack opening is larger than one voxel. It was thus expected that mode I SIF K_I would increase in a more pronounced way. The increase of K_I with loading (especially for scans V_4 and V_5) illustrates higher levels of opening stress intensity near the crack front.

In Fig. 16(b), the consistent and almost unchanged values of K_{II} in scans V_1 to V_3 indicate that the sample underwent very limited mode II contributions. However, a slight increase is observed on the right side in K_{II} values for scans V_4 and V_5, indicating the presence of shear

stresses in that region. The absolute value of K_{III} (Fig. 16 (c)) increases with the applied loading, indicating the presence of tearing stresses. The inclined trends along the sample thickness further highlight an asymmetric distribution of tearing stresses, likely resulting from variations in the loading conditions. Overall, larger values of K_I compared to K_{II} and K_{III} indicate that the deformation was predominantly governed by mode I contributions, with limited influence from modes II and III. In addition, the measured SIFs trends for the last three scans were almost identical, but their levels were much higher than the first five scans. The reasons will be discussed in the next two sections.

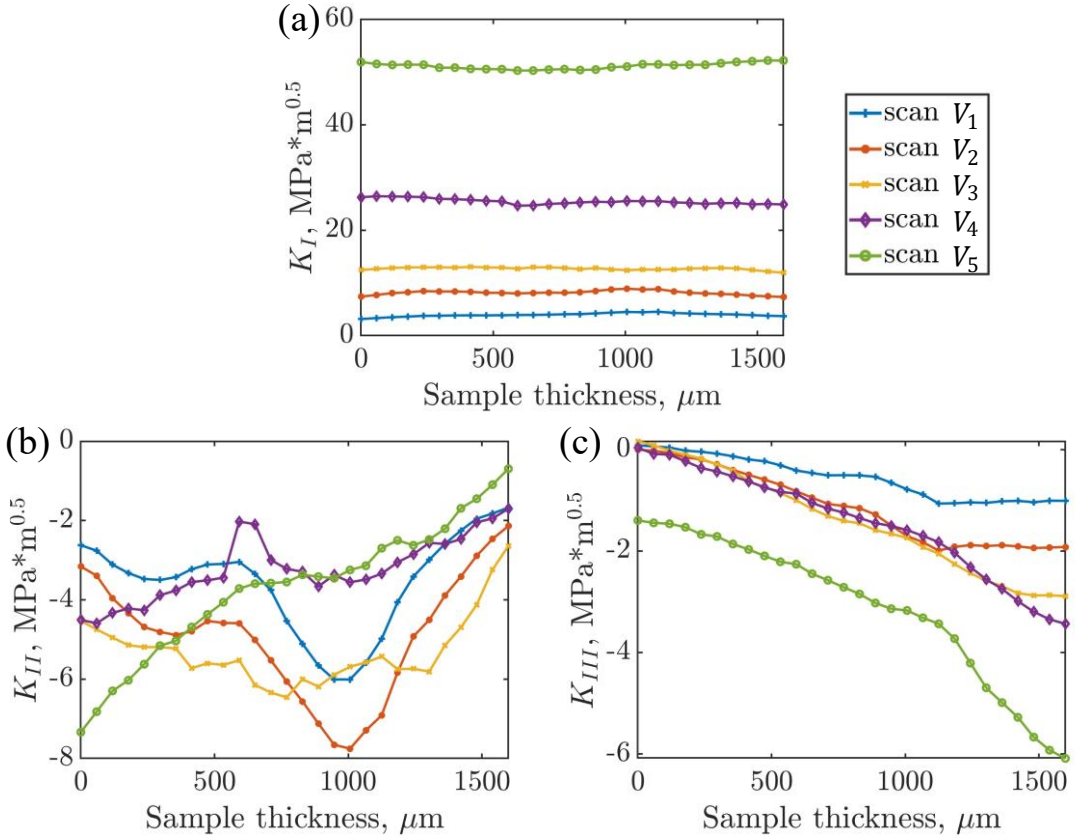

Fig. 16 (a) K_I, (b) K_{II} and (c) K_{III} SIF profiles along the crack front for the first five scans.

5.3.7 Correction of the crack front by Williams' series

The crack fronts in each scan were identified using gray level residuals from DVC and Williams' series, as shown in Fig. 17. A good agreement is observed between the two methods from scans V_1 to V_5, thus indicating the effectiveness of the proposed voxel-scale DVC scheme in locating the crack front when plastic deformation was limited. However, a significant bias occurred in the last three scans (*i.e.*, V_6-V_8) due to the increased presence of plasticity. This bias is attributed to two main factors. First, the presence of more complex deformations

near the crack front is challenging for accurate DVC calculations. It is difficult to fit the crack surface based solely on gray level residuals, especially for the crack front. Second, as discussed previously, the presence of plasticity introduces limitations when using Williams' series, thereby affecting the accuracy of the crack front determination.

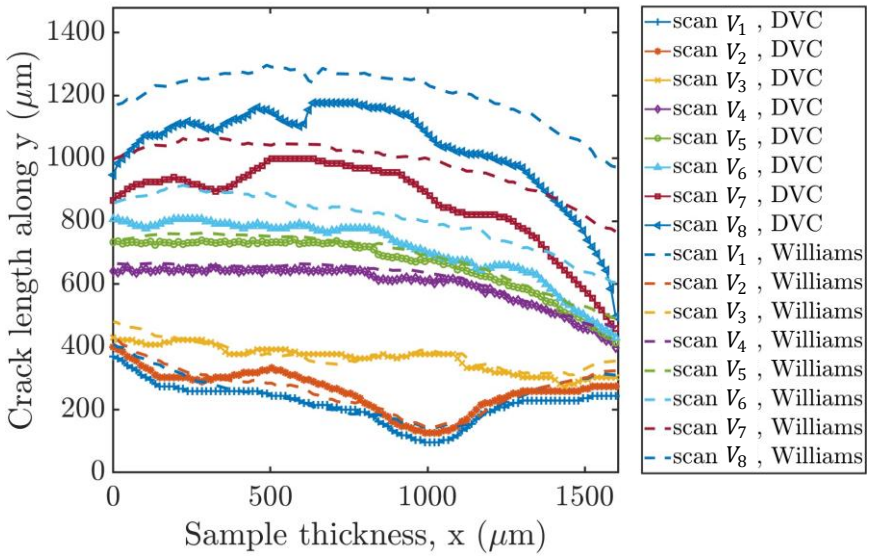

Fig. 17 Crack front for different scans determined by DVC residuals and Williams' series.

5.3.8 Comparison of RMS residuals between Williams' series and DVC measurements

The nodal displacements in each pacman-like plane (as described in Fig. 20 in Appendix B) was obtained based on the Williams' series and DVC measurements, respectively. The corresponding RMS displacement residuals (*i.e.*, $rms(\boldsymbol{u}_W - \boldsymbol{u}_{dvc})$, where $\boldsymbol{u}_W$ is the Williams' series calculated nodal displacements and $\boldsymbol{u}_{dvc}$ the DVC measured one) for each scan are plotted in Fig. 18 (a). The uncertainty level (*i.e.* 0.028 vx as depicted in Fig. 18 (a) in gray line) is defined as 5 times the standard deviation of displacement assessed from the first two scans. Displacement residuals less than the uncertainty level are observed from scans V_1 to V_3, which was expected because of the presence of the crack with sub-voxel opening. For scans V_4 and V_5, displacement residuals are a bit higher than the uncertainty level but still within a low range (*i.e.*, less than 0.07 vx), which indicates that the SIFs evaluation was trustworthy. However, higher displacement residuals with a few tenths of voxel are observed from V_6 to V_8 proving gradual dominance of plasticity near the crack front.

The comparison of gray level residuals (as shown in Fig. 18 (b) and Fig. 21 in Appendix C) between the Williams' series (*i.e.*, gray level residual is calculated by the difference between

the reference volume and deformed volume corrected by the nodal displacements evaluated by Williams' series) and DVC measurements exhibits a consistent trend as analyzed in displacement residuals. Specifically, the difference in RMS gray level residuals remains very small from scans V_1 to V_3, then experiences a slight increase from scans V_4 to V_5, and undergoes a substantial surge from scans V_6 to V_8. The examination of both types of residuals is correlated with plastic activity from scans V_6 to V_8, which explains why only the SIFs up to volume V_5 were reported.

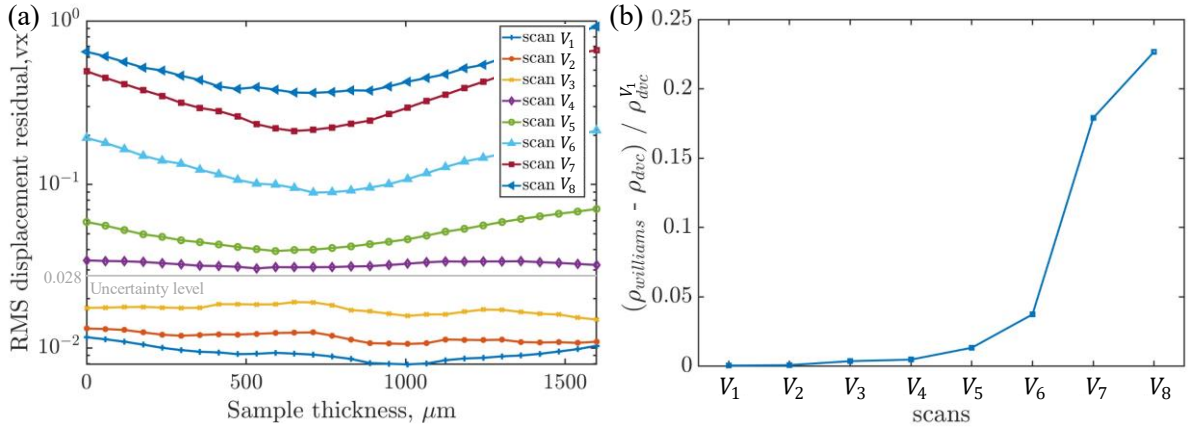

Fig. 18 Residuals comparison for each scan between Williams' series and DVC measurements. (a) RMS displacement residuals along sample thickness. (b) Corresponding difference in RMS gray level residuals.

6. Conclusion

An advanced DVC scheme combined with XCT was employed to investigate 3D crack propagation in nodular graphite cast iron under *in situ* tensile loading. The following main conclusions were drawn from this study:

- Voxel-scale crack analyses based on advanced DVC is a comprehensive methodology for accurately quantifying crack growth. By utilizing a crack growth updating strategy, the crack path and surface were precisely captured even for very large openings. This technique provided valuable insights into the characteristics of 3D crack shape and its propagation, including tendencies to pass around or traverse graphite nodules resulting in a rough cracked surface. Three distinct crack growth stages were identified under dominant mode I loading, namely, crack reopening, crack propagation, and ductile tearing.
- The observed discontinuities in the displacement fields near the crack front indicated

significant crack opening and tearing, which were due to ductile fracture of the sample. Moreover, the von Mises strain fields illustrated the plastic zone surrounding the crack front and its gradual increase with the applied load. The presence of high strain intensifications near the crack tip suggested large deformations and localized stress intensifications.

- CODs extracted from the measured displacement fields provided quantitative insights into crack propagation. The non-uniform distribution of CODs along the sample thickness with a decay toward the crack front, highlighted variations in opening regime. In addition, the entire cracking stages from reopening to ductile tearing was clearly revealed by CODs, thus indicating the efficiency of the proposed framework. However, the presence of substantial plastic deformation near the crack front was challenging in accurately pinpointing the crack front, thereby indicating the need for further advancements in capturing deep cracked regions.
- The estimation of SIFs offered valuable information about stress intensification at the crack front. The dominance of mode I, with limited influences from modes II and III, showed that crack reopening and early propagation occurred under essentially uniform levels along the crack front. Large SIFs in scans with significant crack propagation indicated the gradually more pronounced plasticity. Variations in shear and tearing deformation characteristics along the sample thickness further highlighted the complex distribution during crack growth.

In summary, voxel-scale crack analyses using advanced DVC in conjunction with XCT, provided valuable insights into crack propagation, 3D crack shape, displacement and strain fields, CODs and SIFs. These findings contribute to a better understanding of the crack behavior and mechanical response under *in situ* loading conditions. The reported results also showed deviations from the purely elastic framework based on Williams' series when extensive plastic zones and ductile tearing were observed at the end of the experiment. More advanced models are needed to describe and quantify such phenomena (e.g., via finite element simulations).

Acknowledgements

Dr. N. Limodin and Prof. J.-Y. Buffière kindly provided the precracked sample. Dr. Amine Bouterf performed the *in situ* test. This work has benefited from the support of the French "Agence Nationale de la Recherche" through the "Investissements d'avenir" Program under the reference ANR-10-EQPX-37 MATMECA.

Appendix A. CODs (unit: **μm**) along three directions

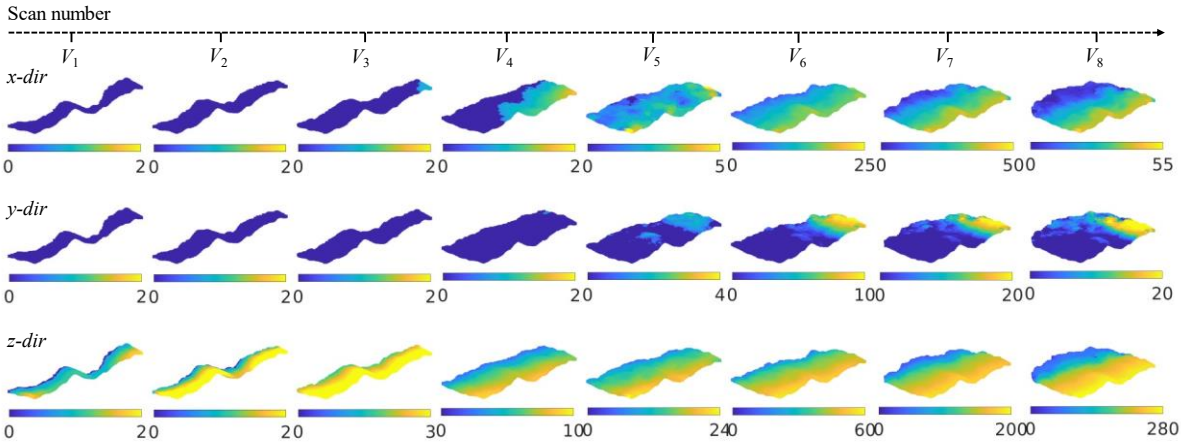

Fig. 19. COD fields for different scans along the *x*-direction (top row), *y*-direction (middle row), and *z*-direction (bottom row). Absolute levels lower than the detection threshold (*i.e.*, 0.6 μm or 0.08 vx) are represented in a distinct deep blue color.

Appendix B. Nodal displacement residuals between Williams series and DVC measurements (unit: vx) along the three directions

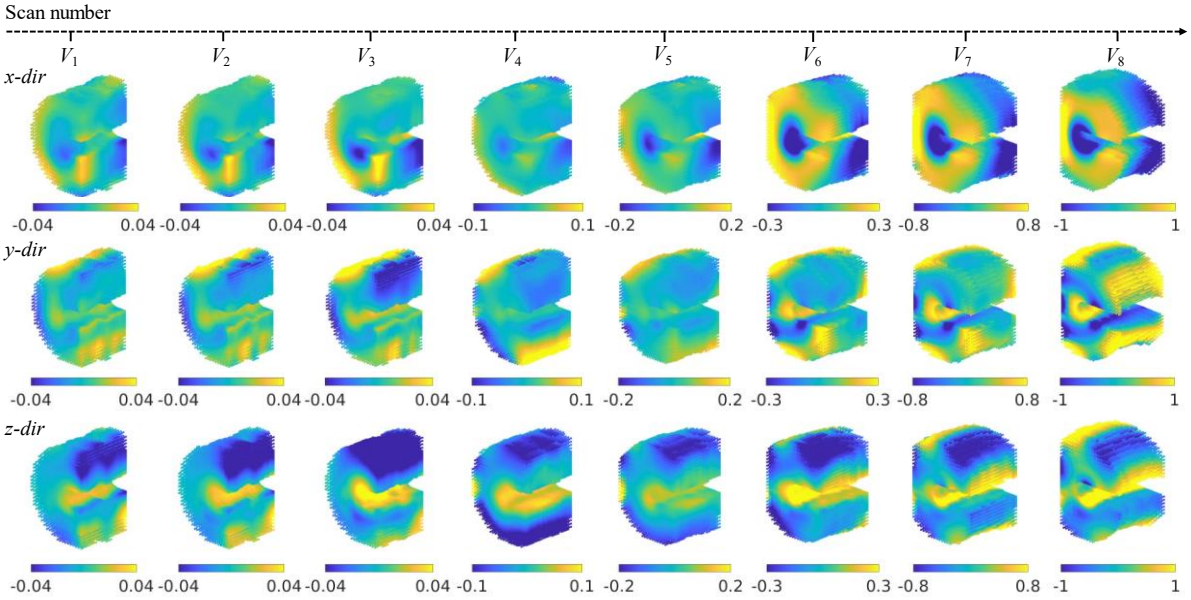

Fig. 20. Nodal displacement residuals for different scans along the *x*-direction (top row), *y*-direction (middle row), and *z*-direction (bottom row). The uncertainty level is 0.028 vx (or 0.21 μm) evaluated from the first two scans.

Appendix C. Element-wise gray level residuals (unit: GL) obtained by Williams series and DVC measurements and their difference

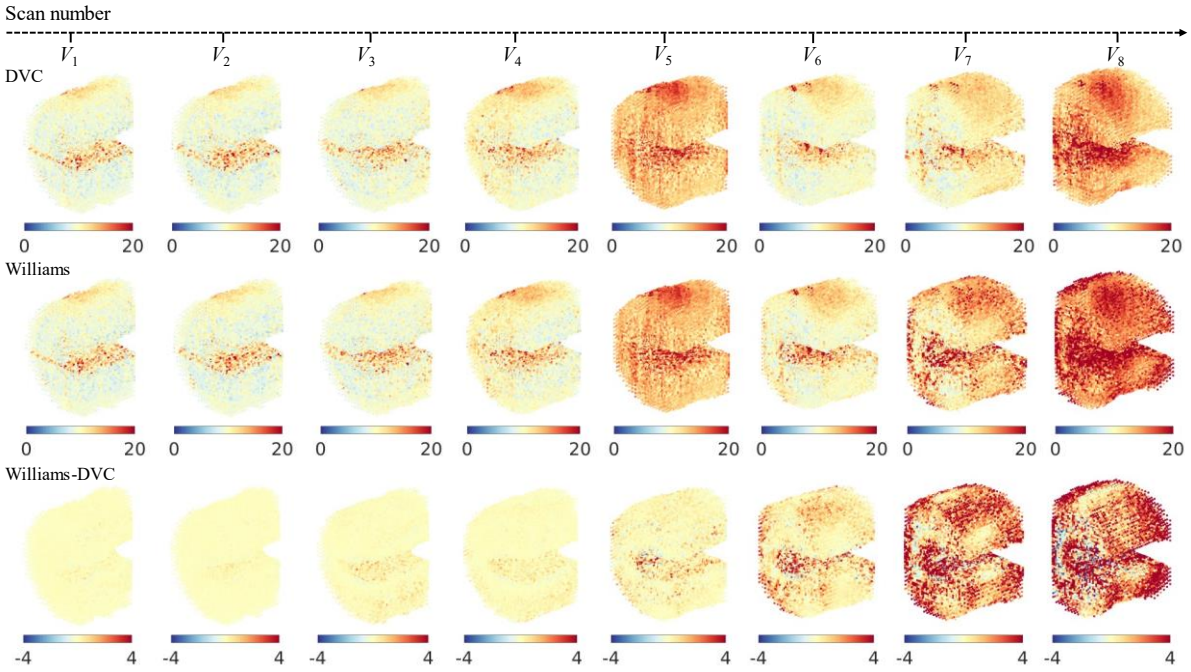

Fig. 21. Element-wise gray level residuals for different scans obtained by DVC (top row), Williams series (middle row), and their differences (bottom row).

References

[1] Lacaze J, Dawson S, Hazotte A. Cast iron: a historical and green material worthy of continuous research. International Journal of Technology. 2021;12:1123-38. https://doi.org/10.14716/ijtech.v12i6.5235.

[2] Paris P, Erdogan F. Closure to "Discussions of 'A Critical Analysis of Crack Propagation Laws'"(1963, ASME J. Basic Eng., 85, pp. 533–534). 1963. https://doi.org/10.1115/1.3656903.

[3] Yates J, Zanganeh M, Tai Y. Quantifying crack tip displacement fields with DIC. Engineering Fracture Mechanics. 2010;77:2063-76. https://doi.org/10.1016/j.engfracmech.2010.03.025.

[4] Becker T, Mostafavi M, Tait R, Marrow T. An approach to calculate the J-integral by digital image correlation displacement field measurement. Fatigue & Fracture of Engineering Materials & Structures. 2012;35:971-84. https://doi.org/10.1111/j.1460-2695.2012.01685.x.

[5] McNeill S, Peters W, Sutton M. Estimation of stress intensity factor by digital image correlation. Engineering fracture mechanics. 1987;28:101-12. https://doi.org/10.1016/0013-7944(87)90124-X.

[6] Gonzáles GL, González JA, Castro JT, Freire JL. A J-integral approach using digital image correlation for evaluating stress intensity factors in fatigue cracks with closure effects. Theoretical and Applied Fracture Mechanics. 2017;90:14-21. https://doi.org/10.1016/j.tafmec.2017.02.008.

[7] Yusof F, Lopez-Crespo P, Withers P. Effect of overload on crack closure in thick and thin specimens via digital image correlation. International Journal of Fatigue. 2013;56:17-24. https://doi.org/10.1016/j.ijfatigue.2013.07.002.

[8] Toda H, Sinclair I, Buffiere J-Y, Maire E, Khor KH, Gregson P, et al. A 3D measurement procedure for internal local crack driving forces via synchrotron X-ray microtomography. Acta Materialia. 2004;52:1305-17. https://doi.org/10.1016/j.actamat.2003.11.014.

[9] Réthoré J, Tinnes J-P, Roux S, Buffière J-Y, Hild F. Extended three-dimensional digital image correlation (X3D-DIC). Comptes Rendus Mécanique. 2008;336:643-9. https://doi.org/10.1016/j.crme.2008.06.006.

[10] Qu P, Toda H, Zhang H, Sakaguchi Y, Qian L, Kobayashi M, et al. Local crack driving force analysis of a fatigue crack by a microstructural tracking method. Scripta materialia. 2009;61:489-92. https://doi.org/10.1016/j.scriptamat.2009.05.004.

[11] Toda H, Maire E, Yamauchi S, Tsuruta H, Hiramatsu T, Kobayashi M. In situ observation of ductile fracture using X-ray tomography technique. Acta Materialia. 2011;59:1995-2008. https://doi.org/10.1016/j.actamat.2010.11.065.

[12] Yang G, Liu C, Liu H. Analysis and Research on Experimental Process of Water Thermal Migration of Freeze–Thaw Cracked Rock Based on Particle Tracking Method and Thermal Imaging Technology. Sustainability. 2023;15(7):5658. https://doi.org/10.3390/su15075658.

[13] Limodina N, Réthoré J, Buffière J Y, Hild F, Roux S, et al. Influence of closure on the 3D propagation of fatigue cracks in a nodular cast iron investigated by X-ray tomography and 3D volume correlation. Acta Materialia, 2010, 58(8): 2957-2967.

[14] Réthoré J, Limodin N, Buffière J-Y, Roux S, Hild F. Three-dimensional analysis of fatigue crack propagation using X-Ray tomography, digital volume correlation and extended finite element simulations. Procedia Iutam. 2012;4:151-8. https://doi.org/10.1016/j.piutam.2012.05.017.

[15] Lachambre J, Réthoré J, Weck A, Buffiere J-Y. Extraction of stress intensity factors for 3D small fatigue cracks using digital volume correlation and X-ray tomography. International Journal of Fatigue. 2015;71:3-10. https://doi.org/10.1016/j.ijfatigue.2014.03.022.

[16] Valle V, Bokam P, Germaneau A, Hedan S. New development of digital volume correlation for the study of fractured materials. Experimental Mechanics. 2019;59:1-15. https://doi.org/10.1007/s11340-018-0415-2.

[17] Jin X, Marrow T J, Wang J, Chen Y, Chen H, Scotson D. Crack propagation in fine grained graphites under mode I and mixed-mode loading, as observed in situ by microtomography. Carbon, 2022; 193: 356-367. https://doi.org/10.1016/j.carbon.2022.03.051.

[18] Jin X, Wade-Zhu J, Chen Y, Mummery P, Fan X, Marrow T. Assessment of the fracture toughness of neutron-irradiated nuclear graphite by 3D analysis of the crack displacement field. Carbon, 2021; 171: 882-893. https://doi.org/10.1016/j.carbon.2020.09.072.

[19] Shen J, Marrow T J, Scotson D, Jin X, Wu H, Chen H. Combined evaluation of Young modulus and fracture toughness in small specimens of fine grained nuclear graphite using 3D image analysis. Journal of Nuclear Materials, 2022; 563: 153642. https://doi.org/10.1016/j.jnucmat.2022.153642.

[20] Chen H, Shen J, Scotson D, Jin X, Wu H, Marrow T. Fracture toughness evaluation of a nuclear graphite with non-linear elastic properties by 3D imaging and inverse finite element analysis. Engineering Fracture Mechanics, 2023; 293: 109719. https://doi.org/10.1016/j.engfracmech.2023.109719.

[21] Koko A, Singh S, Barhli S, Connolley T, Vo NT, Wigger T, et al. 3-Dimensional analysis of fatigue crack fields and crack growth by in situ synchrotron X-ray tomography. International Journal of Fatigue, 2023; 170: 107541. https://doi.org/10.1016/j.ijfatigue.2023.107541.

[22] Bornert M, Brémand F, Doumalin P, Dupré J-C, Fazzini M, Grédiac M, et al. Assessment of digital image correlation measurement errors: methodology and results. Experimental mechanics. 2009;49:353-70. https://doi.org/10.1007/s11340-008-9204-7.

[23] Besnard G, Hild F, Roux S. “Finite-element” displacement fields analysis from digital images: application to Portevin–Le Châtelier bands. Experimental mechanics. 2006;46:789-803. https://doi.org/10.1007/s11340-006-9824-8.

[24] Avril S, Bonnet M, Bretelle A-S, Grédiac M, Hild F, Ienny P, et al. Overview of identification methods of mechanical parameters based on full-field measurements. Experimental Mechanics. 2008;48:381-402. https://doi.org/10.1007/s11340-008-9148-y.

[25] Shakoor M, Buljac A, Neggers J, Hild F, Morgeneyer TF, Helfen L, et al. On the choice of boundary conditions for micromechanical simulations based on 3D imaging. International Journal of Solids and Structures. 2017;112:83-96. https://doi.org/10.1016/j.ijsolstr.2017.02.018.

[26] Tikhonov AN, Arsenin VJ, Arsenin VIAk, Arsenin VY. Solutions of ill-posed problems: Vh Winston; 1977.

[27] Mendoza A, Neggers J, Hild F, Roux S. Complete mechanical regularization applied to digital image and volume correlation. Computer Methods in Applied Mechanics and Engineering. 2019;355:27-43. https://doi.org/10.1016/j.cma.2019.06.005.

[28] Hild F, Bouterf A, Roux S. Damage measurements via DIC. International Journal of Fracture. 2015;191:77-105. https://doi.org/10.1007/s10704-015-0004-7.

[29] Vargas R, Canto R, Smaniotto B, Hild F. Calibration of cohesive parameters for a castable refractory using 4D tomographic data and realistic crack path from in-situ wedge splitting test. Journal of the European Ceramic Society. 2023;43:676-91. https://doi.org/10.1016/j.jeurceramsoc.2022.09.040.

[30] Liu H, Mao L, Ju Y, Hild F. Damage evolution in coal under different loading modes using advanced digital volume correlation based on X-ray computed tomography. Energy. 2023;127447. https://doi.org/10.1016/j.energy.2023.127447.

[31] Liu H, Mao L, Chang X, Hild F. Multiscale Damage Analyses of Red Sandstone in Uniaxial Compression Based on Advanced Digital Volume Correlation. Rock Mechanics and Rock Engineering, 2023; 1-19. https://doi.org/ 10.1007/s00603-023-03504-y.

[32] Buljac A, Jailin C, Mendoza A, Neggers J, Taillandier-Thomas T, Bouterf A, et al. Digital volume correlation: review of progress and challenges. Experimental Mechanics. 2018;58:661-708. https://doi.org/10.1007/s11340-018-0390-7.

[33] Hild F, Bouterf A, Chamoin L, Leclerc H, Mathieu F, Neggers J, et al. Toward 4D mechanical correlation. Advanced Modeling and Simulation in Engineering Sciences. 2016;3:1-26. https://doi.org/10.1186/s40323-016-0070-z.

[34] Claire D, Hild F, Roux S. A finite element formulation to identify damage fields: the equilibrium gap method. International journal for numerical methods in engineering. 2004;61:189-208. https://doi.org/10.1002/nme.1057.

[35] Hild F, Misra A, Dell'Isola F. Multiscale DIC applied to pantographic structures. Experimental Mechanics. 2021;61:431-43. https://doi.org/10.1007/s11340-020-00636-y.

[36] Réthoré J, Roux S, Hild F. An extended and integrated digital image correlation technique applied to the analysis of fractured samples: The equilibrium gap method as a mechanical filter. European Journal of Computational Mechanics/Revue Européenne de Mécanique Numérique. 2009;18:285-306.

https://doi.org/10.3166/ejcm.18.285-306.

[37] Shariati H, Bouterf A, Saadati M, Larsson P-L, Hild F. Probing Constitutive Models of Bohus Granite with In Situ Spherical Indentation and Digital Volume Correlation. Rock Mechanics and Rock Engineering. 2022:1-18. https://doi.org/10.1007/s00603-022-02991-9.

[38] Leclerc H, Périé J-N, Roux S, Hild F. Voxel-scale digital volume correlation. Experimental Mechanics. 2011;51:479-90. https://doi.org/10.1007/s11340-010-9407-6.

[39] Vargas R, Neggers J, Canto RB, Rodrigues J, Hild F. Analysis of wedge splitting test on refractory castable via integrated DIC. Journal of the European Ceramic Society. 2016;36:4309-17. https://doi.org/10.1016/j.jeurceramsoc.2016.07.007.

[40] Hamam R, Hild F, Roux S. Stress intensity factor gauging by digital image correlation: Application in cyclic fatigue. Strain. 2007;43:181-92. https://doi.org/10.1111/j.1475-1305.2007.00345.x.

[41] Roux S, Hild F. Stress intensity factor measurements from digital image correlation: post-processing and integrated approaches. International journal of fracture. 2006;140:141-57. https://doi.org/10.1007/s10704-006-6631-2.

[42] Vargas R, Neggers J, Canto R, Rodrigues J, Hild F. Comparison of two full-field identification methods for the wedge splitting test on a refractory. Journal of the european ceramic society. 2018;38:5569-79. https://doi.org/10.1016/j.jeurceramsoc.2018.07.039.

[43] Limodin N, Réthoré J, Buffière J-Y, Gravouil A, Hild F, Roux S. Crack closure and stress intensity factor measurements in nodular graphite cast iron using three-dimensional correlation of laboratory X-ray microtomography images. Acta materialia. 2009;57:4090-101. https://doi.org/10.1016/j.actamat.2009.05.005.

[44] Affagard J-S, Mathieu F, Guimard J-M, Hild F. Identification method for the mixed mode interlaminar behavior of a thermoset composite using displacement field measurements and load data. Composites Part A: Applied Science and Manufacturing. 2016;91:238-49. https://doi.org/10.1016/j.compositesa.2016.10.007.

[45] Roux S, Réthoré J, Hild F. Digital image correlation and fracture: an advanced technique for estimating stress intensity factors of 2D and 3D cracks. Journal of Physics D: Applied Physics. 2009;42:214004. https://doi.org/10.1088/0022-3727/42/21/214004.

[46] Minguet C, Soulas F, Lafargue-Tallet T, Chalumeau E, Pommies M, Peiffer R, et al. On the validation of a priori estimates of standard displacement uncertainties in T3-stereocorrelation. Measurement

Science and Technology. 2020;32:024004. https://doi.org/10.1088/1361-6501/abafe1.

[47] Hansen PC, Kilmer ME, Kjeldsen RH. Exploiting residual information in the parameter choice for discrete ill-posed problems. BIT Numerical Mathematics. 2006;46:41-59. https://doi.org/10.1007/s10543-006-0042-7.

[48] Anderson TL. Fracture mechanics: fundamentals and applications: CRC press; 2017. https://doi.org/10.1201/9781315370293.